ROYAL SOCIETY OF CHEMISTRY

EDGE ARTICLE

Check for updates

An acetylene-bridged ferrocene macrocycle: efficient synthesis and electron transfer mechanism in mixed-valence systems

Longfei Li,[ab] Beijing Zhang,[ab] Yi Xie,[c] Qi Xiong,[c] Yuanbo Zhong,[ab] Yansong Jiang,[ab] Yu Wang, [ID][ab] Haobing Wang, [ID][ab] Shang-Da Jiang, [ID][c] Shen Zhou [ID] *[d] and Xing Jiang [ID] *[ab]

Cyclic oligomers with multiple redox centers are ideal models for intramolecular electron transfer processes, as they feature well-defined spatial geometries and degenerate energy states. The design and synthesis of such structures with strongly interacting monomers, however, remains a significant challenge. Here, we report a one-pot synthesis of an acetylene-bridged ferrocene macrocycle (**9**) using alkyne metathesis, with a remarkable 43% isolated yield. The macrocycle adopts a chiral *PPM/MMP* conformation in the crystal, reminiscent of the iconic Penrose triangle. Electrochemical studies suggested that redox processes of all three ferrocene units are reversible and highly correlated, despite relatively long Fe–Fe distances. Hydrogenation of acetylene bridges yielded an analogous trimeric ferrocene macrocycle (**14**), whose redox waves showed less separation due to the lack of conjugation and through-bond charge transfer. Assuming that the through-space interaction energy is the same for both macrocycles, we estimated that conjugation through acetylene bridges accounts for 25–36% of overall interaction. Trication **9**$^{3+}$ was obtained by chemical oxidation, and it showed EPR signals with weak anisotropy, indicative of fast intramolecular electron transfer. Varied-temperature (VT) EPR studies suggested intramolecular antiferromagnetic interaction and a doublet ground state ($\Delta E_{D-Q} = -0.06$ kcal mol^{-1}) for **9**$^{3+}$.

Introduction

Mixed-valence compounds, constructed by covalent linkage of redox-active centers in different oxidation states, have been developed to understand key factors of intramolecular charge transfer,[1] an omnipresent process of great significance in biology,[2] catalysis,[3] and materials science.[4] Much attention has been directed to mixed-valence systems of ferrocene (Fc), due to its marvelous stability at the neutral and oxidized states.[5] The synthesis of macrocycles containing multiple Fc units remains challenging due to their high flexibility, which arises from the

facile rotation of cyclopentadienyl (Cp) ligands about the Cp–Fe–Cp axis.[6] So far macrocycles with multiple (≥3) Fc units have been successfully prepared in a limited number of reports,[7–11] among which robust Fc–Fc interactions were observed in merely three systems (Fig. 1a). Santi and Ceccon prepared a "fused" Fc trimer **1** from a triindene trianion and observed two reversible redox events at half-wave potentials ($E_{1/2}$) of 0.23 and 0.61 V, along with a third irreversible oxidation at 0.94 V in cyclic voltammetry (CV).[8] The large half-wave potential split ($\Delta E_{1/2} = 380$ mV) between the first two redox events suggested that they are highly correlated and that **1**$^+$ is at the borderline of class II (partially delocalized) and class III (fully delocalized) mixed-valence systems according to the Robin–Day classification.[12] Albrecht and Long reported an elegant one-pot synthesis of a cyclic Fc pentamer, hexamer, heptamer, and nonamer.[9] Cyclic hexamer **2** was obtained in 2% yield, and it underwent four reversible redox events at $E_{1/2}$ of −0.184, −0.010, 0.365, and 0.933 V. The corresponding $\Delta E_{1/2}$ values of 174, 375, and 568 mV indicated strong interaction and rapid intramolecular electron transfer (∼10^7 s^{-1}) among Fc units. The Gibbs free energy ($\Delta_{int}G$) of Fc–Fc interactions showed a linear dependence on the overall ring charge of **2**. Albrecht and Long also prepared macrocycle **3** with three Fc units, with two of them directly linked to each other and the third separated by phenylene

[a]South China Advanced Institute for Soft Matter Science and Technology, School of Emergent Soft Matter, South China University of Technology, Guangzhou 510640, China. E-mail: xingj@scut.edu.cn

[b]Guangdong Provincial Key Laboratory of Functional and Intelligent Hybrid Materials and Devices, Guangdong Basic Research Center of Excellence for Energy and Information Polymer Materials, South China University of Technology, Guangzhou 510640, China

[c]Spin-X Institute, School of Chemistry and Chemical Engineering, State Key Laboratory of Luminescent Materials and Devices, Guangdong-Hong Kong-Macao Joint Laboratory of Optoelectronic and Magnetic Functional Materials, South China University of Technology, Guangzhou, 511442, China

[d]College of Science, National University of Defense Technology, Changsha, China. E-mail: zhoushen@nudt.edu.cn
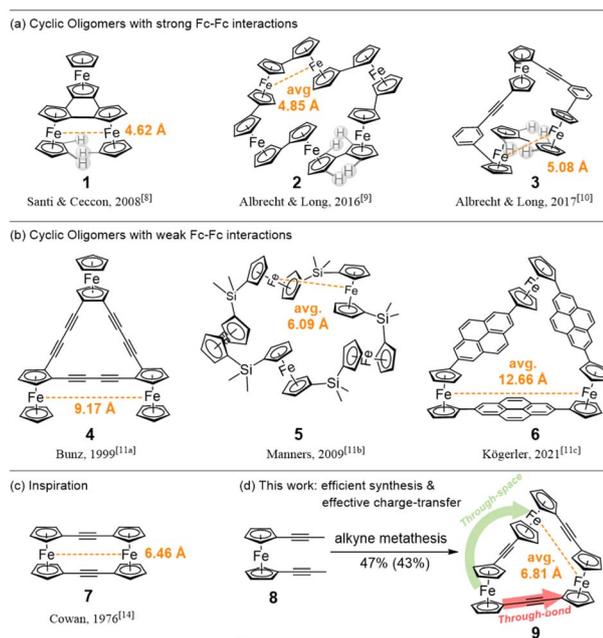
Fig. 1 Representative multi-ferrocene macrocycles with (a) strong and (b) weak electronic interactions; (c) acetylene-bridged macrocycle **7** with a strong electronic interaction and relatively long Fe–Fe distance; (d) the efficient synthesis and effective charge transfer of **9** in this work offering insights into charge transfer mechanisms. Fe–Fe distance was obtained from crystal structures (**1–6**, **9**) or by calculation (**7**).

acetylene bridges.[10] Macrocycle **3** showed three well-defined redox peaks at 0.038, 0.246, and 0.399 V with $\Delta E_{1/2}$ of 208 and 153 mV. The first and third peaks corresponded to the redox processes of the biferrocene (BiFc) moiety, and the second to the isolated Fc. The separation between the first and third peaks (361 mV) was almost identical to that of BiFc (350 mV), suggesting weak interaction between Fc and BiFc moieties in **3**.

We noticed that macrocycles **1–3** all featured directly connected Fc units and short Fe–Fe distances (4.62, 4.85, and 5.08 Å, respectively). This is beneficial for effective charge transfer interaction, which is coulombic in nature and distance-sensitive. Unfortunately, the direct Fc–Fc linkage is sterically crowded and synthetically challenging. The introduction of bridging groups allowed for facile preparation of macrocycles such as **4–6** with improved efficiency; however, the Fe–Fe distance was significantly elongated (9.17, 6.08, and 12.66 Å). Their CV showed poorly resolved or unresolved waves, indicating simultaneous, uncorrelated redox processes of Fc units.[11]

While bridging groups inevitably increase the Fe–Fe distance and weaken through-space interactions,[13] we hypothesized that it might be possible to design a bridged macrocycle with robust Fc–Fc interactions by facilitating through-bond charge transfer. We were inspired by acetylene-bridged macrocycle **7**, whose redox processes are strongly correlated ($\Delta E_{1/2}$ = 355 mV) despite a relatively long Fe–Fe distance of 6.46 Å.[14] The steric repulsion between neighbouring Fc units in macrocycles **1–3** (Fig. 1a) was not observed for **7**, which featured coplanar Cp rings across alkyne bridges. As a result, a delicate balance between the Fe–Fe

distance (through-space) and conjugation (through-bond) was achieved for this macrocycle, and the extent of charge delocalization in **7**[+] is comparable to, if not stronger than, the cations of **1–3**. Since alkyne-bridged macrocycles can be prepared with high efficiency using alkyne metathesis,[15] we decided to explore the synthesis and charge transfer properties of acetylene-bridged multiple-Fc macrocycles. Here, we report the synthesis of an acetylene-bridged ferrocene cyclic trimer as well as its alkene- and alkane-bridged analogues, providing a semi-quantitative analysis of contributions of through-bond and through-space mechanisms in mixed-valence systems for the first time.

Results and discussion

Synthesis and characterization

Alkyne metathesis (AM) of 1,1′-bis(1-propynyl) ferrocene **8**[16] was conducted using a catalyst generated *in situ* from **10** and Ph$_3$-SiOH to yield trimeric macrocycle **9** with high efficiency. Unlike typical rigid building blocks, 1,1′-disubstituted Fc enjoys a high degree of rotational freedom, rendering virtually all cyclic oligomers of different sizes viable products in AM with sufficient thermodynamic stability. Density functional theory (DFT) calculation showed that the relative Gibbs free energies of dimeric (**7**), trimeric (**9**), and tetrameric (**11**) macrocycles are 0, 1.2, and 1.7 kcal mol^{-1}, respectively, suggesting low selectivity in AM. In initial studies, we indeed observed the formation of linear and cyclic tetramers and larger oligomers, along with a major product **9**. Cyclic dimer **7** was detected by mass spectroscopy as a minor product, but we were not able to achieve its isolation. This is consistent with the unique kinetic selectivity of alkyne metathesis.[17] Since the yield of cyclic tetramer **11** was low and its separation was tedious, we focused on improving the selectivity for **9**, by lowering catalyst loading and substrate concentration and avoiding the formation of long-chain oligomers. A 47% NMR yield was eventually achieved under optimized conditions of 10 mM **8** in CHCl$_3$ at 50 °C and 5% catalyst loading (Table S1). Pure product **9** was obtained in 43% yield after column chromatography and subsequent washing with a hexane/DCM mixture. We attributed the unexpected high selectivity for **9** to its low solubility, which was also reflected by its tendency to crystallize.

Since effective charge transfer has also been achieved between Fc units across alkene bridges,[13g,18] we also attempted the synthesis of an analogous macrocycle **13** using olefin metathesis. While **13** was obtained upon treatment of **12** with the Grubbs-II catalyst, we were unable to achieve a reasonable yield (<1%) after multiple rounds of optimization. No other cyclic oligomers were detected. Insoluble materials, presumably ill-defined oligomers, accounted for the mass balance of the reaction. We took this as indirect evidence that alkyne metathesis is superior to olefin metathesis in the assembly of highly dynamic building blocks.[19] Macrocycle **14** with saturated alkane bridges was also prepared for a comprehensive study of the roles of different bridging groups in charge transfer. **14** was obtained in quantitative yield through hydrogenation of macrocycle **9**, using the Pd/C catalyst under 1 atm H$_2$ pressure at
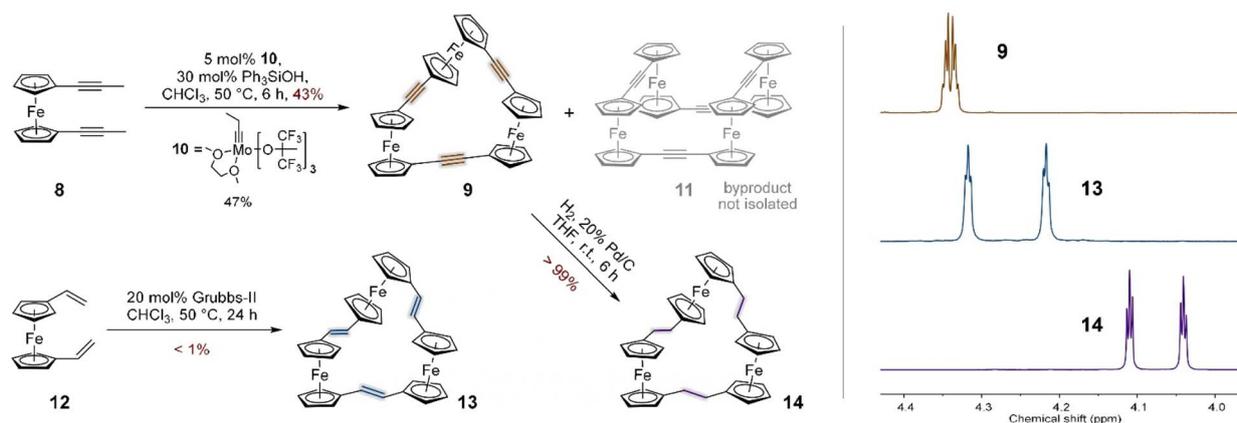
Fig. 2 Synthesis of ferrocene cyclic trimers **9**, **13**, and **14**, and their ^{1}H NMR spectra in CDCl$_3$.

room temperature. Macrocycles **9**, **13**, and **14** were thoroughly characterized by ^{1}H and ^{13}C NMR spectrometry, mass spectrometry, and single crystal X-ray diffraction. It is notable that their solution NMR spectra are rather simple. As shown in Fig. 2, two pseudo-triplets were observed for macrocycles **13** (4.32 and 4.22 ppm) and **14** (4.11 and 4.04 ppm), while they almost merged into one set of signals at 4.35–4.33 ppm for macrocycle **9** in CDCl$_3$. All Fc units appear to be equivalent for each macrocycle in the NMR timescale.

Crystal structures

The structures of all three macrocycles were determined unambiguously by single crystal X-ray diffraction (CCDC 2433325, 2453500, and 2453617). Single crystals were obtained for **9** by slow evaporation of a toluene solution. The crystal structure was solved in the $P3_121$ space group with enriched enantiomer **9$_{PPM}$** as the major component (85%) and the opposite enantiomer **9$_{MMP}$** as a minor, disordered component (15%). The chirality of **9** originated from geometrical constraints enforced by its triangular structure, in which each Fc unit adopts a helical (P/M) conformation. Here, the P/M helicity was defined by viewing along the Cp–Fe–Cp axis and determining whether the far Cp ring needs to rotate clockwise (M) or counterclockwise (P) to overlap with the proximal Cp ring. As shown in Fig. 3a, there are two P-Fc (Fc1 and Fc2) units and one M-Fc (Fc3) in enantiomer **9$_{PPM}$**, whose overall shape is a distorted triangular prism. The three Fe atoms form a triangle with edge lengths of 6.62, 6.65, and 7.15 Å (avg. 6.81 Å) and internal angles of 57.2, 57.6, and 65.3°. The angles between the Cp–Fe Cp axis of Fc units and the Fe–Fe–Fe plane are 62, 63, and 79°. Cp rings of neighbouring Fc units are close to being coplanar, with dihedral angles of 17, 20, and 28°. We also noticed that the two Cp rings are parallel in each Fc unit, and alkyne bond angles are close to 180°, both suggesting the absence of notable ring strain in **9**. These agree well with **9** being a major product in alkyne metathesis with sufficient stability.

The low symmetry of **9$_{PPM}$**/**9$_{MMP}$** suggested that all three Fc units were not equivalent, which contradicted their solution ^{1}H
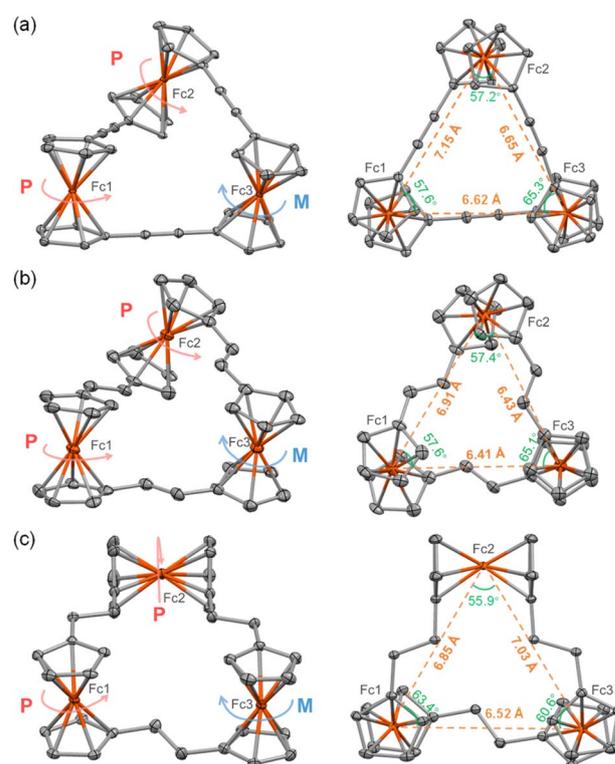

Fig. 3 Side view (left) and top view (right) of the crystal structures of (a) **9**, (b) **13**, and (c) **14**, shown with 30% probability of thermal ellipsoids. Solvent molecules and hydrogen atoms were omitted for clarity. Only one PPM enantiomer was shown for each macrocycle. For full structures, see Fig. S25–S27.

and ^{13}C NMR data. To account for these observations, DFT calculations were performed. We found that despite its apparent rigidity, **9** could undergo isomerization with a low energy barrier, through collective rotation of ferrocene units. As shown in Fig. S33, a 2-fold symmetric transition state (**9-TS**) could be reached from ground-state structures **9-GS1** (**9$_{PPM}$**) or **9-GS2** (**9$_{MMP}$**) through simultaneous rotation of two ferrocene units. The activation barrier for this isomerization was

estimated to be 4.2 kcal mol^{-1}, consistent with rapid isomerization indicated by ^{1}H and ^{13}C NMR spectra. This mode of collective Fc rotation has been reported by Mayor in a rhomboid bisferrocene macrocycle.[7a] It is also worth noting that a minimal change in the Fe–Fe distance was observed between the ground-state (**9-GS1** and **9-GS2**, avg. 6.77 Å) and transition-state structures (**9-TS**, avg. 6.92 Å), highlighting strong geometrical constraints on the Fc units enforced by the macrocycle. Single crystals of **13** were obtained by slow evaporation from a hexane/DCM solution, and its crystal structure was solved in the $P\bar{1}$ space group, featuring a pair of *PPM*/*MMP* enantiomers in a unit cell (Fig. S26). With three *trans*-double bonds as bridges, the overall geometry of **13** resembles that of **9**. Its three Fe atoms are separated by 6.41, 6.43, and 6.91 Å (avg. 6.58 Å), slightly shorter than **9**, with Fe–Fe–Fe angles being 57.4, 57.6, and 65.1°, respectively. The angles between the Cp–Fe–Cp axis of Fc units and the Fe–Fe–Fe plane are 60, 64, and 79°. The alkene-connected Cp rings of adjacent Fc units are characterized by dihedral angles of 19, 19, and 25°.

Single crystals of **14** were also obtained from a hexane/DCM solution, and its crystal structure was solved in a $P\bar{1}$ space group. There were four similar yet unequal pairs of *PPM*/*MMP* enantiomers in a unit cell, highlighting the flexibility of alkane bridges (Fig. S27). The geometric shape of **14** resembles that of **9-TS**, with one of the Fc units (Fc2) perpendicular to the Fe–Fe–Fe plane. The average Fe–Fe distance was found to be 6.80 Å. Since Fe–Fe distances are very close for macrocycles **9**, **13**, and **14** with different bridges, it is possible for us to conduct a straightforward comparison of Fc–Fc interaction within the framework of trimeric macrocycles.

Electrochemistry

The redox properties of macrocycles **9**, **13**, and **14** were studied by cyclic voltammetry. A three-electrode system was used, with a glassy carbon electrode as the working electrode, an Ag/AgCl electrode as the reference electrode, and a Pt sheet electrode as the counter electrode. Solutions at 1.0 mM analyte

Table 1 Electrochemical data for ferrocene macrocycles[a]

Compd	Event	ΔE (V)	$E_{1/2}$ (V)	$\Delta E_{1/2}$ (V)	$K_c{}^b$	$\Delta_c G^c$ (kJ mol^{-1})	$\Delta_{int} G^d$ (kJ mol^{-1})
9[e]	**9/9$^+$**	0.066	0.110				
				0.150	3.43×10^2	−14.47	−17.20
	9$^+$/9^{2+}	0.063	0.260				
				0.161	5.27×10^2	−15.53	−18.26
	9^{2+}/9^{3+}	0.067	0.421				
9[f]	**9/9$^+$**	0.066	0.125				
				0.287	7.10×10^4	−27.69	−30.42
	9$^+$/9^{2+}	0.082	0.412				
				0.376	2.27×10^6	−36.28	−39.00
	9^{2+}/9^{3+}	0.120	0.788				
13[e]	**13/13$^+$**	0.066	−0.105				
				0.166	6.40×10^2	−16.02	−18.74
	13$^+$/13^{2+}	0.070	0.061				
				0.196	2.06×10^3	−18.91	−21.64
	13^{2+}/13^{3+}	0.070	0.257				
13[f]	**13/13$^+$**	0.065	−0.124				
				0.348	7.63×10^5	−33.58	−36.30
	13$^+$/13^{2+}	0.069	0.224				
				0.430	1.86×10^7	−41.49	−44.21
	13^{2+}/13^{3+}	0.082	0.654				
14[e]	—	0.183	−0.092	—	—	—	—
14[f]	**14/14$^+$**	0.063	−0.127				
				0.208	3.28×10^3	−20.07	−22.79
	14$^+$/14^{2+}	0.062	0.081				
				0.229	7.43×10^3	−22.10	−24.82
	14^{2+}/14^{3+}	0.064	0.310				

[a] Conditions: working electrode: glassy carbon; counter electrode: platinum plate; reference electrode: Ag/AgCl; (E *vs.* [Fc]/[Fc$^+$], corrected for iR_s); scan rate: 0.1 V s^{-1}. [b] $K_c = \exp(F\Delta E_{1/2}/RT)$, where F is Faraday's constant and temperature is 25 °C. [c] $\Delta_c G$ refers to the Gibbs free energy of comproportionation, $\Delta_c G = -RT \ln K_c$. [d] $\Delta_{int} G$ refers to the Gibbs free energy of interaction; for three-center systems, $\Delta_{int} G = \Delta_c G - RT \ln 3$. [e] Electrolyte: [$nBu_4$N][PF$_6$]. [f] Electrolyte: [$nBu_4$N][BArF$_{24}$].
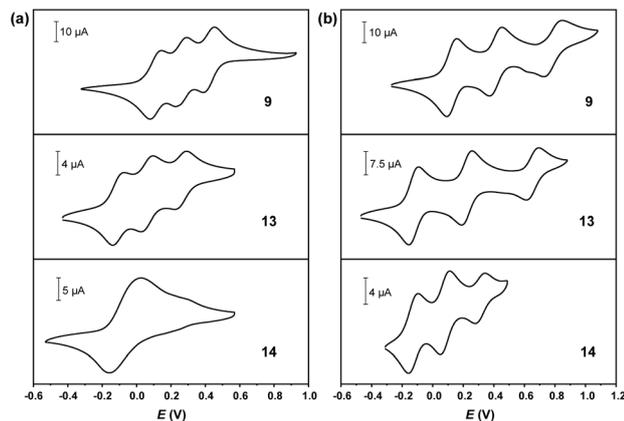
Fig. 4 Cyclic voltammograms for **9**, **13**, and **14** at 1.0 mM in 0.1 M electrolyte/CH$_2$Cl$_2$ (*E vs.* [Fc]/[Fc$^+$]), corrected for iR_s); scan rate: 100 mV s^{-1}. Electrolytes were (a) [nBu$_4$N][PF$_6$] and (b) [nBu$_4$N][BArF$_{24}$].

Fig. 5 Vis/NIR spectra of **9** in CH$_2$Cl$_2$ in its various oxidation states.

concentration were used, with the supporting electrolyte at 0.1 M concentration. All electrochemical data are summarized in Table 1. As shown in Fig. 4a, when [nBu$_4$N][PF$_6$] electrolyte was used, both **9** and **13** exhibited three sets of well-defined redox peaks, attributed to the stepwise oxidation and reduction of three Fc units (Fc/Fc$^+$).

The difference in potentials (ΔE) of each redox event was close to 59 mV, suggesting that they were reversible. The linear fitting of the $i_{pa} - v^{1/2}$ curve at different scan rates proved that these redox processes were diffusion-controlled (Fig. S16–S20).[20] The CV of **14** only showed an unresolved wave. We hence concluded that macrocycles **9** and **13**, with the benefit of conjugation through alkyne and alkene bridges, have a higher degree of charge delocalization than macrocycle **14** upon oxidation. The comproportionation constant (K_c) and free energy of comproportionation ($\Delta_c G$) were calculated to probe the stability of macrocycles at different oxidation states (**MC**$^{n+}$) quantitatively.[21] K_c was found to be on the order of 10^2 and 10^2–10^3 between consecutive redox events of **9** and **13** respectively, with the corresponding $\Delta_c G$ values of −14.47 and −15.53 kJ mol^{-1} for **9** and −16.02 and −18.91 kJ mol^{-1} for **13**, indicating that cations **9$^+$**, **9^{2+}**, **13$^+$**, and **13^{2+}** are thermodynamically stable. The Gibbs free energies of interaction ($\Delta_{int} G$) were calculated following Albrecht and Long's method,[9] yielding values of −17.20 kJ mol^{-1} (**9/9$^+$** − **9$^+$/9^{2+}**), −18.26 kJ mol^{-1} (**9$^+$/9^{2+}** − **9^{2+}/9^{3+}**), −18.74 kJ mol^{-1} (**13/13$^+$** − **13$^+$/13^{2+}**), and −21.64 kJ mol^{-1} (**13$^+$/13^{2+}** − **13^{2+}/13^{3+}**).

$$\mathbf{MC}^{(n-1)} + \mathbf{MC}^{(n+1)} \underset{}{\overset{K_c}{\rightleftharpoons}} 2\mathbf{MC}^{n+}$$

$$K_c = \frac{([\mathbf{MC}^{n+}])^2}{[\mathbf{MC}^{(n-1)+}][\mathbf{MC}^{(n+1)+}]} \tag{1}$$

In order to shed light on the contributions of through-space and through-bond mechanisms to the overall charge transfer, electrochemical studies were performed using [nBu$_4$N][BARF$_{24}$] ([BARF$_{24}$]$^-$ = [B(C$_6$H$_3$(3,5-CF$_3$)$_2$)$_4$]$^-$) as an electrolyte. [BARF$_{24}$]$^-$ is a weaker coordinating anion than [PF$_6$]$^-$ and is incapable of
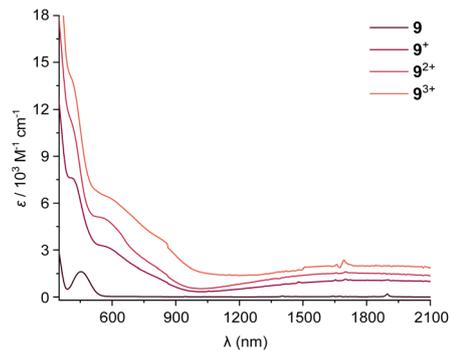
forming strong ion pairs with counterions, thus allowing for a clear observation of otherwise poorly separated redox events.[22] The first oxidation events (**9/9$^+$** and **13/13$^+$**) were not affected by electrolyte, and their $E_{1/2}$ remained the same. In contrast, the subsequent oxidation events were shifted to higher potentials. The corresponding $\Delta E_{1/2}$ values increased to 287 and 376 mV for **9** (150 and 161 mV in [nBu$_4$N][PF$_6$]). A similar change was observed for **13**, and its $\Delta E_{1/2}$ values were 348 mV and 430 mV. We were delighted to observe three sets of well-resolved redox peaks for **14**, with $\Delta E_{1/2}$ = 208 and 229 mV. The interaction energies $\Delta_{int} G$ were found to be −30.42 kJ mol^{-1} and −39.00 kJ mol^{-1} for **9**, −36.30 kJ mol^{-1} and −44.21 kJ mol^{-1} for **13**, and −22.79 and −24.82 kJ mol^{-1} for **14**, respectively. We noted that $\Delta_{int} G$ values were larger for **9** and **13** with through-bond charge transfer across unsaturated bridges, which is absent in **14** with saturated alkane bridges. We hypothesized that the differences in $\Delta_{int} G$ between **9/13** and **14** could be used to quantify such through-bond interactions. Taking **9$^+$** as an example, 75% (−22.79 kJ mol^{-1}) of the overall interaction (−30.42 kJ mol^{-1}) comes from through-space Fc–Fc interactions, and the rest 25% comes from through-bond interactions. This value increased to 36% for **9^{2+}**. The contributions of through-bond interactions across alkenes in **13** were found to be 37% and 44% for **13$^+$** and **13^{2+}**, respectively.

Chemical oxidation and vis/NIR characterization

Considering the stability of the cations of **9**, we attempted to obtain **9$^+$**, **9^{2+}**, and **9^{3+}** by chemical oxidation. This was achieved by slow addition of a CH$_2$Cl$_2$ solution of acetylferrocenium tetrafluoroborate (AcFcBF$_4$, $E_{1/2}$ = 0.27 V, 1.0 or 2.0 equiv.) or tris(4-bromo-phenyl)ammonium hexachloroantimonate (Magic Blue, $E_{1/2}$ = 0.70 V, 3.0 equiv.)[23] to a CH$_2$Cl$_2$ solution of **9** to obtain monocationic, dicationic, or tricationic species. The oxidation processes were confirmed by absorption spectroscopy in the visible and near-infrared (NIR) regions, as shown in Fig. 5. Cations **9$^+$**, **9^{2+}**, and **9^{3+}** exhibited notable similarities in the visible region, with peaks centered at *ca.* 594 nm, which is characteristic of Cp to Fe charge transfer of Fc$^+$.[24] They also displayed strong and rather broad absorptions in the NIR region, akin to **7$^+$** reported by Cowan.[14] The broad peak is likely associated with ligand (acetylene bridge together with Cp) to Fe charge transfer, and the typical intervalence Fc–Fc$^+$ charge
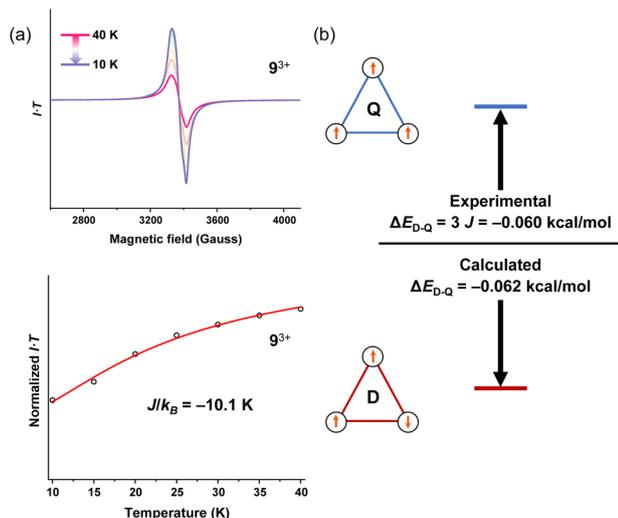
Fig. 6 (a) X-band (9.607 GHz) VT EPR spectra (top) for 9^{3+} powder samples, and plots (bottom) of $I \times T$ (black circles) as a function of T, fitting using eqn (2) (red line); (b) experimental and calculated energy gap between the doublet state (D) and quartet state (Q).

transfer transition was not observed due to its relatively low intensity.

EPR measurements

With a sufficient amount of macrocycle **9** in hand, we proceeded to study its spin properties at different oxidation states, which were not reported for macrocycles **1–3**. Cations 9^+, 9^{2+}, and 9^{3+} were obtained by oxidation with a dichloromethane solution of $AcFcBF_4$ (1.0 or 2.0 equiv.) or an acetonitrile solution of $NOBF_4$ ($\Delta E_{1/2} = 1.00$ V, 3.0 equiv.), followed by vacuum concentration and rinsing with n-hexane. Unfortunately, single crystals were not obtained for these cations. Cation 9^{3+} showed identical cyclic voltammograms to **9** after an initial reduction scan (Fig. S23), which served as circumstantial evidence of the integrity of the macrocycle backbone.
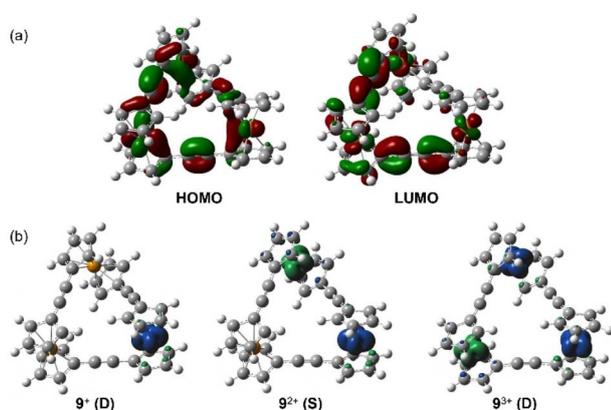

Fig. 7 DFT-calculated (a) frontier molecular orbitals of **9** and (b) its cations spin density at the UPBE0-D3(BJ)/def2-TZVP level; isovalue = 0.005.

At room temperature, X-band EPR spectra of powder samples 9^+ and 9^{2+} displayed one broad signal at $g_\perp = 1.85$ and 1.86, respectively (Fig. S28 and S29). When the temperature was lowered to 10 K, another signal appeared at $g_\parallel = 4.22$ for 9^+ and $g_\parallel = 4.17$ for 9^{2+}. It gave a large g-tensor anisotropy with $\Delta g = 2.37$ for 9^+ and $\Delta g = 2.31$ for 9^{2+} ($\Delta g = g_\parallel - g_\perp$). These features originate from the large orbital angular momentum in Fc, which is similar to those of Fc^+, $BiFc^+$, and $BiFc^{2+}$.[25] We inferred that intramolecular electron transfer in 9^+ and 9^{2+} is slow on the EPR timescale.[26] In stark contrast, the signal of powder samples 9^{3+} at 10 K depicted a relatively sharp peak at $g = 2.038$, with $g_1 = 2.067$, $g_2 = 2.035$, and $g_3 = 2.013$ (Fig. 6). It gave $\Delta g = 0.054$ ($\Delta g = g_1 - g_3$) much less than 0.8, revealing an intramolecular electron transfer rate faster than the EPR time-scale (10^9–10^{10} s^{-1}).[27] Varied-temperature (VT) EPR of 9^{3+} was conducted from 10 to 40 K. The experimental data were analyzed by fitting the $I \times T$ vs. T curve using eqn (2),[28] giving a small anti-ferromagnetic (AFM) exchange coupling constant of $J/k_B = -10.1$ K, with a doublet ground state. The energy gap between the doublet and quartet states (ΔE_{D-Q}) of 9^{3+} was calculated to be $3J = -0.060$ kcal mol^{-1}, which is comparable to other three-center structures in the literature.[29]

$$I \times T = C \left(1 + \frac{4}{1 + \exp\left(-\frac{3J}{kT}\right)} \right) + D \qquad (2)$$

where I is the intensity of the measured EPR signal, T is the temperature, and k is the Boltzmann constant.

Theoretical calculations

We carried out DFT calculations to further our understanding of **9** and its cations. The neutral macrocycle and its cations in the low-spin (LS) or high-spin (HS) configuration were optimized at the UPBE0-D3(BJ)/def2-TZVP theory level. As shown in Fig. 7, the HOMO of **9** mainly consists of the d orbitals of Fe ($d_{x^2-y^2}$ and d_{xy}) and the p (bonding) orbitals of acetylene, while the d orbitals (d_{xy} and d_{yz}) and anti-bonding p orbitals of acetylene contribute to the LUMO. The DFT-optimized structure of **9** overlaid well with the crystal structure (Fig. S32), with nearly identical average Fe–Fe distances of 6.77 and 6.81 Å. Notably, the overall geometry of **9** experienced minor change upon oxidation, and the average Fe–Fe distance first remained the same for **9** and 9^+ and then increased to 6.88 Å (9^{2+}) and 7.11 Å (9^{3+}). The spin density of cations of **9** is almost localized in Fe atoms, and Mulliken spin population analysis shows that the spin populations of 9^+, 9^{2+}, and 9^{3+} are 0.000, 0.001, 1.338; 0.004, -1.346, 1.346; and 1.363, -1.363, 1.363, respectively. These revealed that 9^{2+} adopts a singlet ground state, and 9^{3+} exhibits a doublet ground state. The calculated energy gaps between low-spin and high-spin states (ΔE_{LS-HS}) for 9^{2+} and 9^{3+} were -0.016 and -0.062 kcal mol^{-1}, which is consistent with experimental results, suggesting they both exhibit AFM interactions. Furthermore, we calculated the ΔE_{S-T} value of $BiFc^{2+}$ and 7^{2+} (Fig. S34), which also have singlet ground states and small energy gaps of -0.086 and -0.242 kcal mol^{-1}, consistent with literature reports.[30]

Conclusions

In summary, a trimeric ferrocene macrocycle **9** with an intriguing Penrose-stairs-like chiral structure was synthesized *via* alkyne metathesis in 43% isolated yield. Cyclic trimers **13** and **14**, with similar Fe–Fe distances yet different bridging groups, were also prepared. Electrochemical studies suggested the essential role of through-bond interactions across the bridges. A semi-quantitative analysis suggested that the contribution of through-bond charge transfer across the alkyne bridge is 25–36% and 37–44% across the alkene bridge. VT-EPR measurements and DFT calculations suggested that trication **9**$^{3+}$ is anti-ferromagnetic, with a ΔE_{D-Q} of -0.06 kcal mol^{-1}.

Author contributions

Conceptualization: X. J.; data curation: L. L., B. Z., Y. X., Q. X., and Y. J.; analysis: all authors; supervision: S.-D. J., S. Z., and X. J.; writing – original draft: X. J. and L. L.; writing – review & editing: all authors.

Conflicts of interest

There are no conflicts to declare.

Data availability

CCDC 2433325, 2453500 and 2453617 contain the supplementary crystallographic data for this paper.[31–33]

The supporting data of this manuscript are available in the SI. See DOI: **https://doi.org/10.1039/d5sc02322j**.

Acknowledgements

Notes and references

1 (a) K. D. Demadis, C. M. Hartshorn and T. J. Meyer, *Chem. Rev.*, 2001, **101**, 2655–2686; (b) P. Day, N. S. Hush and R. J. H. Clark, *Philos. Trans. R. Soc., A*, 2008, **366**, 5–14; (c) J. Hankache and O. S. Wenger, *Chem. Rev.*, 2011, **111**, 5138–5178; (d) A. Heckmann and C. Lambert, *Angew. Chem., Int. Ed.*, 2012, **51**, 326–392; (e) Y. Zhong, C. Liu and J. R. Reimers, *Mixed-Valence Systems: Fundamentals, Synthesis, Electron Transfer, and Applications*, VCH, Weinheim, 2023.

2 (a) A. M. Kuznetrsov, *Charge transfer in physics, chemistry and biology: physical mechanisms of elementary processes and an introduction to the theory*, CRC Press, Boca Raton, 2020; (b) L. Zhang, Z. Xie, Z. Liu, S. Zhou, L. Ma, W. Liu, J.-W. Huang, T.-P. Ko, X. Li, Y. Hu, J. Min, X. Yu, R.-T. Guo and C.-C. Chen, *Nat. Commun.*, 2020, **11**, 2676; (c) N. Wang, H. Gao, Y. Li, G. Li, W. Chen, Z. Jin, J. Lei, Q. Wei and H. Ju, *Angew. Chem., Int. Ed.*, 2021, **60**, 197–201; (d) R. R. Nazmutdinov, S. A. Shermokhamedov, T. T. Zinkicheva, J. Ulstrup and X. Xiao, *Chem. Soc. Rev.*, 2023, **52**, 6230–6253.

3 (a) A. Garci, J. A. Weber, R. M. Young, M. Kazem-Rostami, M. Ovalle, Y. Beldjoudi, A. Atilgan, Y. J. Bae, W. Liu, L. O. Jones, C. L. Stern, G. C. Schatz and J. F. Stoddart, *Nat. Catal.*, 2022, **5**, 524–533; (b) P. G. Barros, J. Derosa, M. J. Chalkley and J. C. Peters, *Nature*, 2022, **609**, 71–76; (c) J. Lee and W. J. Song, *J. Am. Chem. Soc.*, 2023, **145**, 5211–5221.

4 (a) Y. Wang, S. Wang, X. Wang, W. Zhang, W. Zheng, Y.-M. Zhang and S. X.-A. Zhang, *Nat. Mater.*, 2019, **18**, 1335–1342; (b) B. Li, K. Kumar, I. Roy, A. V. Morozov, O. V. Emelyanova, L. Zhang, T. Koç, S. Belin, J. Cabana, R. Dedryvère, A. M. Abakumov and J.-M. Tarascon, *Nat. Mater.*, 2022, **21**, 1165–1174; (c) Y.-K. Qu, D.-Y. Zhou, Q. Zheng, P. Zuo, Z.-L. Che, L.-S. Liao and Z.-Q. Jiang, *Angew. Chem., Int. Ed.*, 2024, **63**, e202408712.

5 (a) D. O. Cowan, C. L. Vanda, J. Park and F. Kaufman, *Acc. Chem. Res.*, 1973, **6**, 1–7; (b) F. Jäkle and J. B. Sheridan, *Ferrocenes: ligands, materials and biomolecules*, ed. P. Stepnicka, VCH, Weinheim, 2008, vol. 1; (c) K. Heinze and H. Lang, *Organometallics*, 2013, **32**, 5623–5625; (d) D. Astruc, *Eur. J. Inorg. Chem.*, 2017, **1**, 6–29.

6 (a) D. Braga, *Chem. Rev.*, 1992, **92**, 633–665; (b) J. D. Dunitz, *Acta Crystallogr., Sect. B: Struct. Sci., Cryst. Eng. Mater.*, 1995, **51**, 619–631; (c) M. Appel, B. Frick, T. L. Spehr and B. Stühn, *J. Chem. Phys.*, 2015, **142**, 114503.

7 (a) B. Grossmann, J. Heinze, E. Herdtweck, F. H. Kohler, H. Noth, H. Schwenk, M. Spiegler, W. Wachter and B. Weber, *Angew. Chem., Int. Ed.*, 1997, **36**, 387–389; (b) T. Fukino, N. Fujita and T. Aida, *Org. Lett.*, 2010, **12**, 3074–3077; (c) T.-H. Chen, W. Kaveevivitchai, N. Bui and O. S. Miljanic, *Chem. Commun.*, 2012, **48**, 2855–2857; (d) V. Hoffmann, L. L. Pleux, D. Haussinger, O. T. Unke, A. Prescimone and M. Mayor, *Organometallics*, 2017, **36**, 858–866; (e) S. A. Sheppard, T. L. R. Bennett and N. J. Long, *Eur. J. Inorg. Chem.*, 2022, **13**, e202200055; (f) B. Lan, J. Xu, L. Zhu, X. Chen, H. Kono, P. Wang, X. Zuo, J. Yan, A. Yagi, Y. Zheng, S. Chen, Y. Yuan, K. Itami and Y. Li, *Precis. Chem.*, 2024, **2**, 143–150; (g) J. Xu, B. Lan, L. Zhu, H. Xu, X. Chen, W. Li, Y. Yuan, J. Yan and Y. Li, *Chem. Res. Chin. Univ.*, 2024, **40**, 881–886.

8 S. Santi, L. Orian, A. Donoli, A. Bisello, M. Scapinello, F. Benetollo, P. Ganis and A. Ceccon, *Angew. Chem., Int. Ed.*, 2008, **47**, 5331–5334.

9 M. S. Inkpen, S. Scheerer, M. Linseis, A. J. P. White, R. F. Winter, T. Albrecht and N. J. Long, *Nat. Chem.*, 2016, **8**, 825–830.

10 L. E. Wilson, C. Hassenrgck, R. F. Winter, A. J. P. White, T. Albrecht and N. J. Long, *Angew. Chem., Int. Ed.*, 2017, **56**, 6838–6842.

11 (a) U. H. F. Bunz, G. Roidl, M. Altmann, V. Enkelmann and K. D. Shimizu, *J. Am. Chem. Soc.*, 1999, **121**, 10719–10726;

(b) D. E. Herbert, J. B. Gilroy, W. Chan, L. Chabanne, A. Staubitz, A. J. Lough and I. Manners, *J. Am. Chem. Soc.*, 2009, **131**, 14958–14968; (c) M. Metzelaars, S. Sanz, J. Rawson, R. Hartmann, C. M. Schneiderb and P. Kögerler, *Chem. Commun.*, 2021, **57**, 6660–6663.

12 M. B. Robin and P. Day, *Adv. Inorg. Chem. Radiochem.*, 1967, **10**, 247–422.

13 (a) C. C. Allen and N. S. Hush, *Prog. Inorg. Chem.*, 1967, **8**, 357–389; (b) B. Mayoh and P. Day, *J. Am. Chem. Soc.*, 1972, **94**, 2885–2886; (c) C. Creutz, *Prog. Inorg. Chem.*, 1983, **30**, 1–73; (d) H. Taube, *Angew Chem. Int. Ed. Engl.*, 1984, **23**, 329–339; (e) J. R. Reimers and N. Hush, *Inorg. Chem.*, 1990, **29**, 3686–3697; (f) C. Joachim, J. P. Launay and S. Woitellier, *Chem. Phys.*, 1990, **147**, 131–141; (g) J.-P. Collin, P. Laine, J.-P. Launay, J.-P. Sauvagea and A. Sour, *J. Chem. Soc., Chem. Commun.*, 1993, **5**, 434–435; (h) A.-C. Ribou, J.-P. Launay, M. L. Sachtleben, H. Li and C. W. Spangler, *Inorg. Chem.*, 1996, **35**, 3735–3740.

14 C. Levanda, K. Bechgaard and D. O. Cowan, *J. Org. Chem.*, 1976, **41**, 2700–2704.

15 (a) D. Lee, I. Volchkov and S. Y. Yun, Alkyne Metathesis, *Org. React.*, 2020, **102**, 613–931; (b) S. Huang, Z. Lei, Y. Jin and W. Zhang, *Chem. Sci.*, 2021, **12**, 9591–9606; (c) A. Fürstner, *J. Am. Chem. Soc.*, 2021, **143**, 15538–15555.

16 J. Ma, N. Krauße and H. Butenschön, *Eur. J. Org Chem.*, 2015, **20**, 4510–4518.

17 X. Jiang, J. D. Laffoon, D. Chen, S. Pérez-Estrada, A. S. Danis, J. Rodríguez-López, M. A. Garcia-Garibay, J. Zhu and J. S. Moore, *J. Am. Chem. Soc.*, 2020, **142**, 6493–6498.

18 M. Hisatome, O. Tachikawa, M. Sasho and K. Yamakawa, *J. Organomet. Chem.*, 1981, **217**, C17–C20.

19 Y. Jin, A. Zhang, Y. Huang and W. Zhang, *Chem. Commun.*, 2010, **46**, 8258–8260.

20 A. J. Bard, L. R. Faulkner and H. S. White, *Electrochemical methods: fundamentals and applications*, VCH, Weinheim, 2022.

21 (a) S. Barlow and D. O'Hare, *Chem. Rev.*, 1997, **97**, 637–669; (b) B. S. Brunschwig and N. Sutin, *Coord. Chem. Rev.*, 1999, **187**, 233–254; (c) D. M. D'Alessandro and F. R. Keene, *Chem. Soc. Rev.*, 2006, **35**, 424–440; (d) D. M. D'Alessandro and F. R. Keene, *Chem. Rev.*, 2006, **106**, 2270–2298; (e) S. Santi, A. Bisello, R. Cardena and A. Donoli, *Dalton Trans.*, 2015, **44**, 5234–5257.

22 (a) F. Barrière, N. Camire, W. E. Geiger, U. T. Mueller-Westerhoff and R. Sanders, *J. Am. Chem. Soc.*, 2002, **124**, 7262–7263; (b) F. Barrière and W. E. Geiger, *J. Am. Chem. Soc.*, 2006, **128**, 3980–3989; (c) W. E. Geiger and F. Barrière, *Acc. Chem. Res.*, 2010, **43**, 1030–1039.

23 N. G. Connelly and W. E. Geiger, *Chem. Rev.*, 1996, **96**, 877–910.

24 (a) C. LeVanda, D. O. Cowan, C. Leitch and K. Bechgaard, *J. Am. Chem. Soc.*, 1974, **96**, 6788–6789; (b) D. M. Duggan and D. N. Hendrickson, *Inorg. Chem.*, 1975, **14**, 955–970.

25 (a) R. Prins and F. J. Reinders, *J. Am. Chem. Soc.*, 1969, **91**, 4929–4931; (b) R. Prins, *Mol. Phys.*, 1970, **19**, 603–620; (c) D. O. Cowan, G. A. Candela and F. Kaufman, *J. Am. Chem. Soc.*, 1971, **93**, 3889–3893; (d) W. H. Morrison and D. N. Hendrickson, *Inorg. Chem.*, 1975, **14**, 2331–2346.

26 (a) T.-Y. Dong, D. N. Hendrickson, C. G. Pierpont and M. F. Moore, *J. Am. Chem. Soc.*, 1986, **108**, 963–971; (b) T.-Y. Dong, T. Kambara and D. N. Hendrickson, *J. Am. Chem. Soc.*, 1986, **108**, 4423–4432; (c) T.-Y. Dong, L.-S. Chang, G.-H. Lee and S.-M. Peng, *Organometallics*, 2002, **21**, 4192–4200; (d) D. Siebler, C. Förster, T. Gasi and K. Heinze, *Organometallics*, 2011, **30**, 313–327.

27 (a) T.-Y. Dong, C.-C. Schel, M.-Y. Hwang, T.-Y. Lee, S.-K. Yeh and Y.-S. Wen, *Organometallics*, 1992, **11**, 573–582; (b) T.-Y. Dong, P.-H. Ho, X.-Q. Lai, Z.-W. Lin and K.-J. Lin, *Organometallics*, 2000, **19**, 1096–1106; (c) T. Sixt, M. Sieger, M. J. Krafft, D. Bubrin, J. Fiedler and W. Kaim, *Organometallics*, 2010, **29**, 5511–5516.

28 (a) O. Kahn, *Molecular Magnetism*, VCH, New York, 1993, p. 211; (b) D. Zhang, Z. Zhu, X. Xiao, Y.-H. Fang, T. Xiao, X. Wang, S.-D. Jiang and D. Zhao, *J. Am. Chem. Soc.*, 2024, **146**, 21752–21761; (c) D. Zhang, Z. Zhu, X. Xiao, H. Han, L. Meng, H. Yu, X. Fu and D. Zhao, *CCS Chem.*, 2025, **7**, 1834–1843; (d) Y. Shi, X. Li, J. Di, Y. Xue, N. Zhang, T. Jin, C.-F. Chen, P. Chen, *CCS Chem.*, ASAP, DOI: **10.31635/ccschem.024.202404995**.

29 (a) T. Itoh, K. Matsuda, H. Iwamura and K. Hori, *J. Am. Chem. Soc.*, 2000, **122**, 2567–2576; (b) S. Suzuki, A. Nagata, M. Kuratsu, M. Kozaki, R. Tanaka, D. Shiomi, K. Sugisaki, K. Toyota, K. Sato, T. Takui and K. Okada, *Angew. Chem., Int. Ed.*, 2012, **51**, 3193–3197; (c) Y. Wu, M. D. Krzyaniak, J. F. Stoddart and M. R. Wasielewski, *J. Am. Chem. Soc.*, 2017, **139**, 2948–2951; (d) Y. Hattori, E. Michail, A. Schmiedel, M. Moos, M. Holzapfel, I. Krummenacher, H. Braunschweig, U. Meller, J. Pflaum and C. Lambert, *Chem.–Eur. J.*, 2019, **25**, 15463–15471; (e) C. Luo, Y. Zhao, T. Wang, Q. Sun, R. Pei, Y. Zhao, Y.-Z. Zheng and X. Wang, *J. Am. Chem. Soc.*, 2023, **145**, 17292–17298; (f) H. Han, Y. Huang, C. Tang, Y. Liu, M. D. Krzyaniak, B. Song, X. Li, G. Wu, Y. Wu, R. Zhang, Y. Jiao, X. Zhao, X.-Y. Chen, H. Wu, C. L. Stern, Y. Ma, Y. Qiu, M. R. Wasielewski and J. F. Stoddart, *J. Am. Chem. Soc.*, 2023, **145**, 18402–18413; (g) S. Tang and X. Wang, *Angew. Chem., Int. Ed.*, 2024, **63**, e202310147; (h) A. Borissov, P. J. Chmielewski, A. C. Valdivia, C. J. Gómez-García, J. Casado and M. Stępień, *Angew. Chem., Int. Ed.*, 2024, **63**, e202408510.

30 (a) J. A. Kramer and D. N. Hendrickson, *Inorg. Chem.*, 1980, **19**, 3330–3337; (b) H. Hilbig, P. Hudeczek, F. H. Köhler, X. Xie, P. Bergerat and O. Kahn, *Inorg. Chem.*, 1998, **37**, 4246–4257; (c) T. Mochida, T. Akasaka, Y. Funasako, Y. Nishio and H. Mori, *Cryst. Growth Des.*, 2013, **13**, 4460–4468.

31 L. Li, B. Zhang, Y. Xie, Q. Xiong, Y. Zhong, Y. Jiang, Y. Wang, H. Wang, S.-D. Jiang, S. Zhou and X. Jiang, CCDC 2453500: Experimental Crystal Structure Determination, 2025.

32 L. Li, B. Zhang, Y. Xie, Q. Xiong, Y. Zhong, Y. Jiang, Y. Wang, H. Wang, S.-D. Jiang, S. Zhou and X. Jiang, CCDC 2453500, *Experimental Crystal Structure Determination*, 2025.

33 L. Li, B. Zhang, Y. Xie, Q. Xiong, Y. Zhong, Y. Jiang, Y. Wang, H. Wang, S.-D. Jiang, S. Zhou and X. Jiang, CCDC 2453617, *Experimental Crystal Structure Determination*, 2025.